



Research paper

Ce_{0.70}La_{0.20}Ni_{0.10}O_{2-δ} catalyst for methane dry reforming: Influence of reduction temperature on the catalytic activity and stability



Lidia Pino*, Cristina Italiano, Antonio Vita, Massimo Laganà, Vincenzo Recupero

CNR Istituto di Tecnologie Avanzate per l'Energia "Nicola Giordano", Via S. Lucia 5, 98126, Messina, Italy

ARTICLE INFO

Article history:

Received 21 April 2017

Received in revised form 20 June 2017

Accepted 26 June 2017

Available online 8 July 2017

Keywords:

Methane dry reforming

Ni-lanthana-ceria solid solution

Metal support interaction

Catalyst stability

ABSTRACT

The influence of reduction temperature (450–900 °C) on the catalytic activity of Ce_{0.70}La_{0.20}Ni_{0.10}O_{2-δ} sample during methane dry reforming reaction to synthesis gas has been studied. The activity of the sample, prepared by combustion synthesis, has been evaluated at 750 °C under increasing gas hourly space velocity (from 26400 to 105600 h⁻¹) for 50 h of stream. H₂-reduction of the sample at 450 °C induces, during reaction, large amount of carbon deposition (21–27%) that increases by increasing the gas hourly space velocity (GHSV), as revealed by TPO analysis on spent catalysts. Stable activity was revealed after reduction at 750 and 900 °C under a GHSV of 26400 h⁻¹. The catalytic activity of the reduced samples, by apparent specific activity, increases by increasing the Ni particles size and by increasing the fraction of Ni sites revealed by H₂-TPD peak at high temperature.

The catalytic behavior has been discussed on the basis of the samples characterizations derived from X-ray diffraction, UV–vis diffuse reflectance spectroscopy, H₂-programmed reduction (TPR) and desorption (TPD), CO pulse chemisorption, X-ray photoelectron spectroscopy (XPS) and Scanning Electron Microscopy–Energy dispersive X-Ray (SEM/EDX).

© 2017 Elsevier B.V. All rights reserved.

1. Introduction

Dry reforming of methane (CH₄ + CO₂ ↔ 2CO + 2H₂, ΔH₂₉₈ = 260.5 kJ/mol) has received recently growing interest from the view point of global-warming prevention because utilizes the greenhouses gas, mainly responsible of the climate changes observed during the recent decades [1]. Agriculture, waste and energy production are the main sectors that contribute significantly to the methane emissions in the atmosphere; only the waste sector contributes with about 5% to the global greenhouse budget [2]. Currently, the most common strategy applied in the waste management is landfilling, this leads to the generation of methane and carbon dioxide by anaerobic degradation of the organic matter; whereby landfill gas or biogas utilization in a process like dry reforming can offer valuable environmental benefit with, in the same time, the valorization of both gases.

In addition, carbon dioxide reforming of methane becomes industrially advantageous if compared with partial oxidation and steam reforming process for synthesis gas production; this is due to the resulting H₂/CO ratio close to one, appropriate for gen-

erate renewable energy via the gas-to-liquid technology such as Fischer–Tropsch synthesis for liquid hydrocarbons production or to produce oxygenate compounds (methanol) [3–6]. The high endothermicity of dry reforming reaction is furthermore suitable to store the abundant thermal solar or nuclear energy as chemical energy in the chemical energy transmission systems (CETS); solar/nuclear energy can be used to convert CH₄ and CO₂ to synthesis gas, that can be stored or transported off-site where the energy sources are limited. The energy stored in syngas may be liberated by the backward reaction and employed as energy source [7–9].

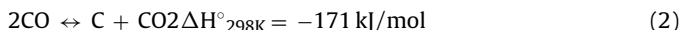
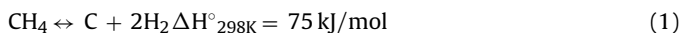
Despite the above mentioned applications, the industrial development of dry reforming has not yet found implementation because of the rapid deactivation of the catalyst due to coke formation.

Nobel metals (Rh, Ru, Pt and Ir) can provide good catalytic performance in terms of activity, selectivity and resistance to carbon deposition, but the limited reserves and the high cost of this materials restricts their applicability [10]. Ni-based catalysts, characterized by extensive availability and low cost can be considered as good replacement to noble metals with promising performance in dry reforming reaction [11]. Nevertheless, these catalytic systems are highly sensitive to coke deposition, induced by methane

* Corresponding author.

E-mail address: lidia.pino@itaec.cnr.it (L. Pino).

decomposition (1) and CO disproportionation or Boudouard reaction (2):



methane decomposition is favored at high temperatures and low pressures, while the Boudouard reaction is favored at low temperatures and high pressures [12–14].

Various approaches including: a) support's effect [15–18], b) support and catalyst preparation methods [19–23], c) addition of promoters and doping with other metals [24–28] have been therefore investigated to improve the catalytic performance of Ni-based catalysts.

CeO₂ and CeO₂-mixed oxides, as supports for Ni catalysts, have been extensively studied during the past several years [29–32]; the high oxygen storage capacity (OSC) of this metal oxides, based on the ability to undergo reversible redox transitions forming non stoichiometric phases CeO₂ → CeO_{2-x}, can increase the resistance to carbon formation. Besides, this characteristic can modify the properties of the supported metal by strong metal-support interactions (SMSI). The SMSI effect, firstly reported by Tauster et al. [33] for metal supported on TiO₂, has been reported also for ceria supported noble metal, induced by the reduction treatments [34]. Different explanations are given in literature for this phenomenon: electronic metal-support interactions, prevailing for low reduction temperature (≤500 °C) [35,36], and decoration or encapsulation of metal by partially reduced ceria, for reduction temperature higher than 700 °C [37]. Recently, the morphology changes induced under strongly reducing conditions has been observed also for Ni-ceria catalysts and ascribed to a similar SMSI effect [38–40]. DFT calculations and Photoemission spectroscopy have demonstrated, for this Ni-CeO₂ system, the co-existence of Ni²⁺/Ni⁺ species and partially reduced ceria [41,42]. M. Fernández-García and coworkers [43] pointed out as the Ni-Ce interface, related to the uncoordinated metal atoms, brings a beneficial rule in many catalytic processes: decreases the methanation activity of Ni under water gas shift reaction, induces high activity during bio-alcohols reforming. The addition of surface modifiers of ceria (ZrO₂, La₂O₃, Pr₂O₃) can induce further changes in the interface between metal and oxides phases, influencing the activity of the resulting catalysts. The relation between activity and structural modification as results of the treatment in reducing atmosphere, in the case of ceria-lanthana support, is not fully understood yet; whereby to investigate this important effect is crucial, in order to develop new catalysts for dry reforming reaction.

In this study we evaluated the structural, redox and catalytic properties of Ce_{0.70}La_{0.20}Ni_{0.10}O_{2-δ} (Ni = 3.66 wt%) catalyst after the H₂/N₂ treatment at three different temperatures, 450, 750 and 900 °C, aiming to study the influence of this properties on the catalyst activity and stability. The related samples have been characterized in calcined and reduced form by X-ray diffraction, UV–vis diffuse reflectance spectroscopy, H₂-programmed reduction (TPR) and desorption (TPD), CO pulse chemisorption, X-ray photoelectron spectroscopy and Scanning Electron Microscopy-Energy dispersive X-Ray (SEM/EDX). The catalytic activity and stability of the samples have been evaluated at increasing gas hourly space velocity, from 26400 to 105600 h⁻¹, along 50 h of time on stream. Temperature programmed oxidation (TPO) of the spent samples has been applied in order to estimate the carbon deposition.

2. Experimental

2.1. Catalyst preparation

The 3.66wt%Ni/La₂O₃–CeO₂ sample, synthetically represented as Ce_{0.70}La_{0.20}Ni_{0.10}O_{2-δ}, was prepared by combustion synthesis, details of the preparation procedure has been previously reported [44]. An aqueous solution, containing (NH₄)₂Ce(NO₃)₆·6H₂O, La(NO₃)₃·6H₂O and Ni(NO₃)₂·6H₂O as metal precursors, and oxalylhydrazide (C₂H₆N₄O₂, all reagents from Aldrich) as fuel, was homogenized and transferred in an oven furnace heated to 350 °C. The water evaporation, followed by self-ignition and combustion of the remaining mixture resulting in the formation of a foamy powder. The obtained powder was then heated at 600 °C in air for 1 h to burn off any carbonaceous residues of the sample, then pelletized, crushed and sieved to different grain size. For comparison a sample without nickel, Ce_{0.78}La_{0.22}O_{2-δ}, has been prepared following the same procedure.

2.2. Catalysts characterizations

Powder XRD patterns were recorded on a Philips X-Pert 3710 diffractometer, using a CuKα radiation (λ=1.5406 Å) at 40 kV and 30 mA. Continuous scans were collected with a scan rate of 1.5° min⁻¹ within the range 20° < 2θ < 75°; while a scan rate of 0.06° min⁻¹ in the 2θ range 27.5–29.5 and 42.5–45.5, was applied to highlight the Ce(111) and Ni(111) reflections, respectively. The lattice parameter (α) was derived according to the following equation and related to a cubic structure:

$$\alpha = \sqrt{h^2 + k^2 + l^2} d_{hkl} \quad (3)$$

The mean crystallite size (d) was related to the pure X-ray broadening (β) by the Scherrer equation:

$$d = \frac{K_\lambda}{\beta \cos \theta} \quad (4)$$

the half maximum line width from pure CeO₂ (111) and Ni(111) reflecting planes were used.

The UV–vis diffuse reflectance spectra were recorded on a Agilent Cary Series UV–vis-NIR spectrophotometer equipped with an integration sphere; before making the measurements, for samples in powder form, the reflectance of BaSO₄ was used as blank sample (reference) to perform the instrument baseline correction. All spectra were collected in diffuse reflectance mode, in the range 200–800 nm at room temperature, and transformed to a magnitude proportional to the extinction through the Kubelka-Munk function. Besides, to separate the contribution of the support in the catalyst, the reflectance R(λ) of the sample was made proportional to the reflectance of the catalysts and the Kubelka-Munk function F(R_∞) was derived.

Temperature programmed reduction (TPR) tests were carried out in a flow system by using a Micromeritics 2750 instrument equipped with a TCD detector. A mixture of 5% H₂/Ar (30 ml min⁻¹) was flowed into the system, the temperature was raised up to the reduction temperature (450, 750 and 900 °C) with a rate of 20 °C min⁻¹ and maintained to the selected temperature for 2 h. The H₂ consumption was monitored by the TCD detector calibrated with standard gas. This procedure has been adopted in order to mimic the reaction's conditions applied during the catalytic experiments. After reduction, the samples were cooled at room temperature in 5% H₂/Ar mixture and held for 1 h, purged in Ar gas flow for removing the reversibly adsorbed H₂. When the baseline of TCD became stabilized, temperature programmed desorption (TPD) of hydrogen was carried out heating the samples up to 900 °C (20 °C min⁻¹) under Ar flow [32,45,46]. The dispersion of reduced nickel was derived as 2·(area of TPD)/(area of TPR);

the apparent Ni particle size (d_{Ni}) was derived from the dispersion measurement, according to the following equation:

$$d_{Ni} (nm) = \frac{0.97}{D(\%)} \times 100 \quad (5)$$

The nickel dispersion was derived by CO-pulse chemisorption method, as reported by Takeguchi et al. [47], with the same apparatus described for TPR-TPD analysis. The samples were reduced in the same conditions adopted to evaluate the catalytic activity; then three steps were carried out, at room temperature, before CO-chemisorption: (1) oxidation under pure O₂ flow (30 Nml min⁻¹) for 10 min; (2) treatment under CO₂ flow (30 Nml min⁻¹) for 10 min; (3) reduction under pure H₂ flow (30 Nml min⁻¹) for 30 min; with this procedure the CO adsorption on CeO₂, as carbonate species, is avoided. After that, the CO-chemisorption was performed at 25 °C.

X-ray photoelectron spectra of the sample powders were collected on a PHI Spectrometer (model 5800-01) equipped with an electron flood gun neutralizer and a monochromatic AlK α -source, operating a 350 W. Measurements were carried out with a constant pass energy of 11.75 eV; before spectral acquisitions, the samples were out-gassed overnight in the preparation chamber of the spectrometer. The characteristic photoemission peaks from O(1s), C(1s), Ni(3p), La(3d) and Ce(3d) core levels were recorded for each sample; the C1s peak at 284.8 eV was used as reference for energy corrections. Peak fitting involved a deconvolution with the use of mixed Gaussian-Lorentzian or Gaussian (for Ni3p) functions. Both peak fitting and chemical analysis, as chemical composition, were carried out by using the PHI Multipak v.6 software.

The morphological features of the fresh (reduced) and spent catalysts were examined by Scanning Electron Microscopy (SEM) with a FEI XL30 microscope equipped with a field emission gun and EDX probe, operating at an accelerating voltage of 20 kV.

The carbon deposition, occurring during the catalytic testing, was evaluated by temperature programmed oxidation (TPO) with the Micromeritics instrument previously described. The samples pre-treated with He, were oxidized in 5%O₂/N₂ mixture (30 ml min⁻¹) raising the temperature from ambient to 1000 °C under a rate of 10 °C min⁻¹; the amount of carbon deposited on the catalytic surface was determined by measuring the CO₂ produced and analyzed by a quadrupole mass spectrometer (QMS Thermo Scientific ProLab).

2.3. Catalysts testing

Activity tests were carried out in a fixed bed quartz reactor (6 mm i.d.) at 750 °C under atmospheric pressure with a feed containing CH₄:CO₂:N₂ = 1:1:0.5 (molar ratio). The catalysts, diluted with quartz sand (catalyst:quartz sand = 1:3) and holed between two plugs of quartz wool, were located in the central section of the reactor, placed in an electric furnace. The reaction temperature was measured/controlled by two k-thermocouples, located into and outside the catalytic bed, respectively. The gaseous feed (CH₄, CO₂, N₂ and H₂ for the reduction step) was controlled by mass flow controller (Brooks Instr.). Reagents and reaction products were analyzed with an on-line gas chromatograph (Agilent 6890 Plus) equipped with FID and TCD detectors. Preliminary tests have been carried out by changing the flow rate of the reagents mixtures (from 30 to 100 ml min⁻¹) under a constant gas hourly space velocity (GHSV = 26400 h⁻¹) and the grain size of the catalyst (150–600 μ m) in order to investigate the diffusion effect on the CH₄ conversion. The reforming rate results almost constant with a gas flow rate higher than 70 ml min⁻¹ for catalyst with grain size between 200–300 μ m. The catalysts were pre-reduced in situ with a 25%H₂/N₂ (80 ml min⁻¹) mixture at various temperature in the range 450–900 °C. The required temperature was reached at a rate

of 10 °C min⁻¹ and maintained for 2 h; after reduction the catalytic bed was purged with a flow of N₂ gas and the reactor was then set to the reaction temperature (750 °C). The catalytic activity has been evaluated at different GHSV (26400, 52800 and 105600 h⁻¹). Reagents conversion (X) and H₂/CO molar ratio are defined as follows:

$$X_{CH_4} = \frac{F_{CH_4,in} - F_{CH_4,out}}{F_{CH_4,in}} \times 100 \quad (6)$$

$$X_{CO_2} = \frac{F_{CO_2,in} - F_{CO_2,out}}{F_{CO_2,in}} \times 100 \quad (7)$$

$$\frac{H_2}{CO} = \frac{F_{H_2}}{F_{CO}} \quad (8)$$

where F is the molar flow rate of reagents species measured at inlet or at outlet of the reactor, respectively.

3. Results

3.1. Characterization of catalysts

3.1.1. X-ray diffraction (XRD)

The XRD patterns of the catalyst, in calcined form and after the reduction step at increasing temperature, are depicted in Fig. 1. The Bragg diffraction peaks of CeO₂ and NiO, scarcely visible, can be observed; this, associated with the absence of La₂O₃ diffraction peaks, suggests the formation of a complex solid solution Ni-La-Ce-Ox, as previous reported [44]. The formation of solid solution can be derived from the change of position for the main reflection peaks related to pure ceria and highlighted in the inset I of Fig. 1 for the 2 θ range 27.5–29.5°. The shift to lower 2 θ angles indicates the distortion of the ceria lattice with a concomitant increase in the lattice parameter (α); this can be due to the partial substitution of Ce⁴⁺ ions (ionic radius = 0.097 nm) by larger La³⁺ (0.116 nm) and smaller Ni²⁺ (0.081 nm) cations. The derived lattice parameter α = 0.5445 nm, reported in Table 1, results higher than the corresponding value ascribed to pure ceria cell (α_{CeO_2} = 0.5411 nm), confirming the formation of a mixed oxides phase.

The theoretical estimate of the lattice parameter related to doped ceria, with the concurrent creation of oxygen vacancies, can be derived by application of the following equation, proposed by Hong and Virkar [48]:

$$\alpha = \frac{4}{\sqrt{3}} \{x_d r_d + (1 - x_d) r_{Ce} + (1 - 0.25x_d) r_O + (0.25x_d r_{Vo})\} 0.9971 \quad (9)$$

where x_d is the molar fraction of dopants, r_d is the ionic radius of dopants; r_O and r_{Vo} represent the radii of an O²⁻ ion and oxygen vacancy in four-fold coordination, respectively. Using the corresponding ionic radius of the dopants ($r_{La^{3+}}$ = 0.116 nm and $r_{Ni^{2+}}$ = 0.081 nm), r_O = 0.138 nm (for four-fold coordination), r_{Vo} = 0.1164 nm (derived by the authors through a number of measurements) and the correction factor 0.9971 (account for the observed difference in the experimental/calculated values from the ionic radii for the lattice parameter of pure ceria), a theoretical value of 0.5447 nm for the current sample can be derived. On this basis, the calculated lattice parameter results in sufficient accordance with the experimental value giving an indirect evidence of the solid solution formation.

The H₂-reduction of the catalyst induces a further shift to lower angles of the CeO₂ reflections, that increases by increasing the reduction temperature; as consequence, the lattice parameter (α) progressively increases, as evidenced in Table 1. The NiO reflections obviously disappear; while the Ni(111) reflection peaks, with intensity that slightly increases by increasing the reduction temperature, where evidenced, as depicted in the inset II of Fig. 1. This can suggest a most high content of metallic nickel; while, from the

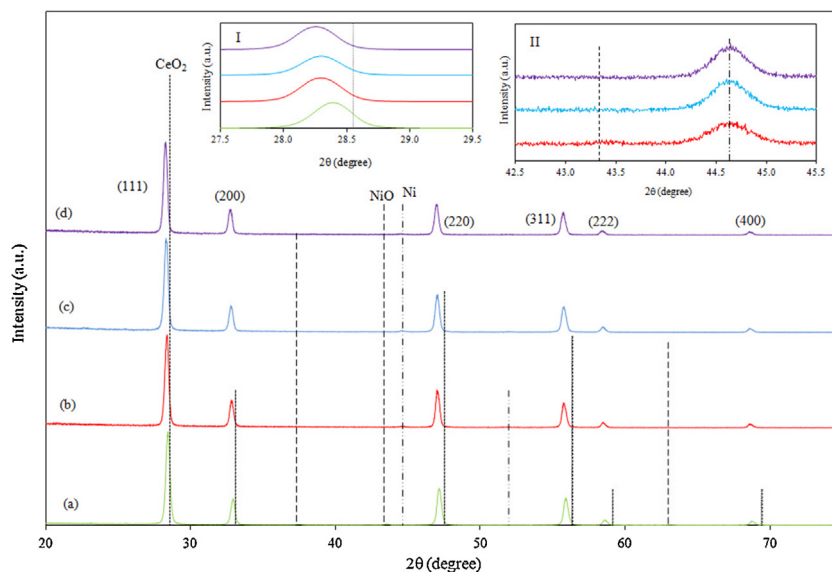


Fig. 1. XRD patterns of the $\text{Ce}_{0.70}\text{La}_{0.20}\text{Ni}_{0.10}\text{O}_{2-\delta}$ catalyst in calcined form (a) and after the pre-reduction at increasing temperature: b) 450 °C; c) 750 °C; d) 900 °C, compared with the reference compounds (JCPDF files 4–593 for CeO_2 , 4–835 for NiO and 4–850 for Ni). In the inserts the magnification of the regions $27.5^\circ < 2\theta < 29.5^\circ$ (Inset I) and $36^\circ < 2\theta < 45^\circ$ (Inset II) respectively, are included.

Table 1
Physical properties of the $\text{Ce}_{0.70}\text{La}_{0.20}\text{Ni}_{0.10}\text{O}_{2-\delta}$ sample in calcined form and after the H_2 -reduction step.

Sample	Particle size (nm) ^a			CeO_2 lattice parameter, α (nm) ^b	CeO_2 $\Delta 2\theta$ shift degree ^c
	CeO_2	NiO	Ni		
Calcined	23.2	–	–	0.5445	0.1834
$T_{\text{reduction}} = 450^\circ\text{C}$	21.9	–	18.9	0.5462	0.2734
$T_{\text{reduction}} = 750^\circ\text{C}$	22.2	–	20.5	0.5463	0.2754
$T_{\text{reduction}} = 900^\circ\text{C}$	22.2	–	21.0	0.5471	0.3194

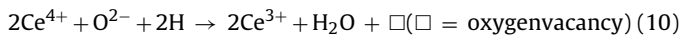
^a Evaluated from CeO_2 , NiO and Ni (111) reflections according to the Scherrer equation.

^b From CeO_2 (111) reflection by application of the equation $\alpha = \sqrt{h^2 + k^2 + l^2} d_{hkl}$.

^c Derived by comparison with JCPDS file for the (111) reticular plane ($\Delta 2\theta$ = peak position of CeO_2 like phase in the mixed oxide – peak position of the reference CeO_2).

decrease in the peak broadening, a weak sintering of the particles induced by the H_2 treatment can be derived as shown in Table 1. The increase in the lattice parameter by increasing the reduction temperature suggests a further solubility of the host cations in the ceria lattice associated with the partial reduction of Ce^{4+} to Ce^{3+} . The ionic radius of Ce^{3+} (0.114 nm) larger than Ce^{4+} can contribute to the increase in the observed α parameter. Besides, insertion in the solid of hydride ion H^- (0.154 nm), that may substitute an anionic vacancy O^{2-} (0.132 nm), can further contribute to the observed lattice expansion. The CeMe_xO_y ($\text{M} = \text{Ni}, \text{Cu}$) catalytic system, treated under H_2 atmosphere and appropriate temperature, can be considered a large hydrogen reservoir (H^* species), as widely reported by Jalowiecki-Duhamel and coworkers [49–51]. The related mechanism, suggested by the authors, includes the succession of more steps, synthesized as:

a) ceria reduction by the H_2 dissociated on metal with formation of oxygen vacancies



b) heterolytic splitting of H_2



one half of the defined hydrogen reservoir (H^*) consists of hydride ions H^- and the other half is proton H^+ , provided by the hydroxyl group (OH^-)

c) the formed hydroxyl groups can recombine together forming H_2O and restoring the anionic vacancies



The substitution of anionic vacancy (O^{2-}) with hydride ion (H^-), together with the contribution of reduced cations, determines the lattice expansion observed by the authors after H_2 -treatment of the samples at temperature higher than 400 °C. The observed mechanism can also account in the current samples; indeed, the co-presence of trivalent La^{3+} and divalent Ni^{2+} cations can further increase the formation of extrinsic vacancies in the solid facilitating the equilibrium of oxygen atoms between the surface and the bulk.

3.1.2. UV-vis

UV-vis diffuse reflectance spectroscopy has been applied to obtain information about the coordination environment, electronic states of the metal ions, together with the energy gap of the metal oxide. Fig. 2a presents the UV-vis DR spectra of the studied catalyst in the calcined form and after the reduction treatment at different temperatures; the spectra are compared with the analogous spectrum of the support ($\text{Ce}_{0.78}\text{La}_{0.22}\text{O}_{2-\delta}$). A very careful observation reveals that the support exhibits three absorption maxima in the range 200–400 nm; these peaks, centered at around 260, 320 and 340 nm, correspond to the charge-transfer transitions $\text{O}^{2-} \rightarrow \text{Ce}^{3+}$, $\text{O}^{2-} \rightarrow \text{Ce}^{4+}$ and interband transition, respectively. In pure CeO_2 the $\text{O}^{2-} \rightarrow \text{Ce}^{4+}$ and interband transition occur generally at about 278 and 313 nm, respectively [52,53]; the red shift (higher wavelength) in the observed bands can be explained as a defect-induced intro-

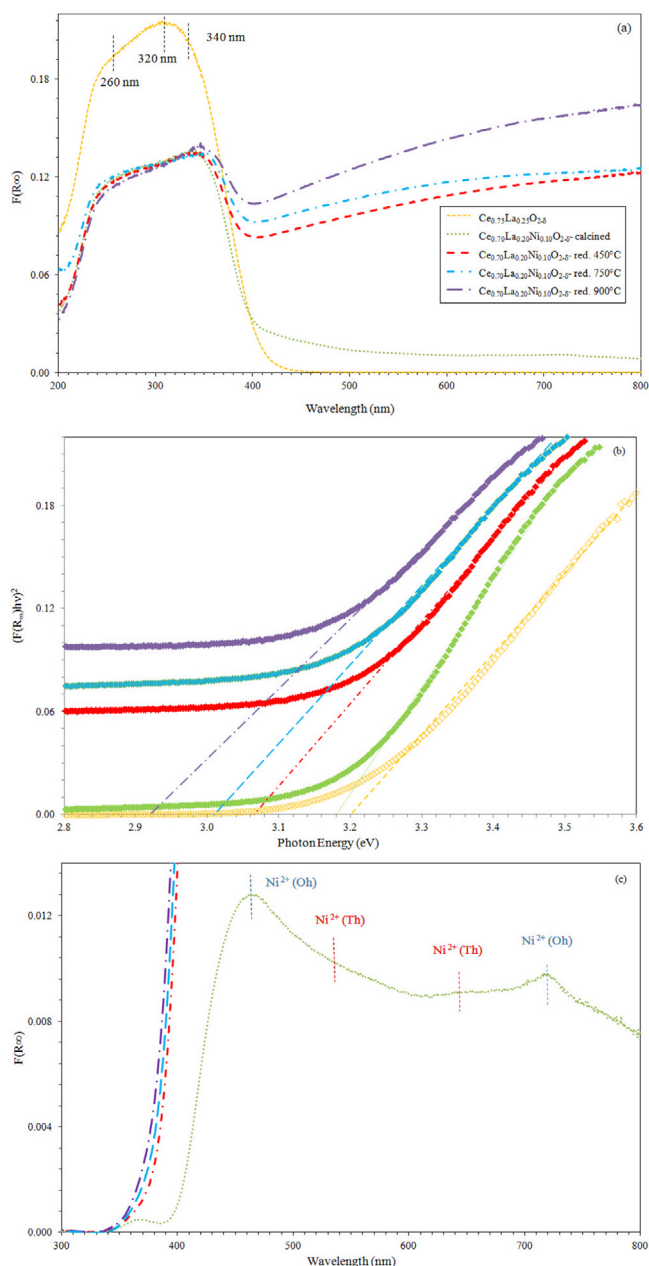


Fig. 2. UV-vis/DR spectra of the studied catalyst after the different H_2 -treatments compared with the support (a); relative Tauc's plot (b) and DR spectra after subtraction of the support contribution.

duction of energy levels into the interband gap, due to the doping with transition metal ions, in accordance with the literature [54,55]. Moreover the characteristic $O^{2-} \rightarrow Ce^{3+}$ charge transfer band, sufficiently resolved, can imply the occurrence of oxygen vacancy defects in the sample caused by introduction of La^{3+} cations in the ceria fluorite structure [56,57]. This evidence, coupled with the observed lattice expansion derived from XRD analysis, confirms the dissolution of large La^{3+} ions into the CeO_2 lattice.

The nickel addition to the Ce-La-Ox catalytic system induces noticeable changes in the spectra: the broadening of the $O^{2-} \rightarrow Ce^{3+}$ and $O^{2-} \rightarrow Ce^{4+}$ charge transfer bands, the decrease in the relative intensity of the bands ($O^{2-} \rightarrow Ce^{4+}$)/($O^{2-} \rightarrow Ce^{3+}$) and the red shift of the band evidenced at 340 nm, that overlaps with the NiO charge transfer band (350 nm) [58]. Besides, weak d-d band in the 400–800 nm range and ascribed to differently coordinated Ni^{2+} , were also observed. Both evidences as the broadening

of the bands and the change in the relative intensity of the ($O^{2-} \rightarrow Ce^{4+}$)/($O^{2-} \rightarrow Ce^{3+}$) bands may be due to the increasing number of surface defects; similarly the red shift suggests an increase in the content of the oxygen vacancies; from this evidence a partial incorporation of Ni^{2+} in the Ce-La-Ox support can be predicted.

The H_2 -treatment of the sample at increasing temperature determines a further red shift of the band evidenced at 340 nm that increases by increasing the reduction temperature (from 450 to 900 °C). Besides, a high absorption band in the 400–800 nm range, due to the surface plasmon resonance effect related to the formation of metallic nickel nanoparticles, can be observed [59].

As widely reported in literature [60,61], in a semiconductor oxide like CeO_2 , the adsorption at high wavelength, due to the introduction of energy levels in the interband gap, implies a decrease in the band gap of the materials. The band gap energies of support and catalysts differently treated has been determined by using the intercept of the tangent to the graph (Tauc's plot), obtained by plotting the square root of the Kubelka-Munk function multiplied by the photon energy ($[F(R_{\infty})h\nu]^2$) versus the photon energy ($h\nu$), as shown in Fig. 2b. Accordingly to the plots, the band gap was estimated to be 3.20 eV and 3.18 eV for the calcined support and catalyst, respectively; a further decrease in the band gap value to 3.07, 3.01 and 2.92 eV, by increasing the reduction temperature from 450 to 900 °C, was observed. The band gap energy of CeO_2 is reported to be 3.6 eV; this value sensitively decreases by doping: a decrease from 3.24, 3.27 and 2.5 eV has been reported for Ni, Co and Ni-Co codoping samples [62]. Thurber et al. [63] found that the band gap energy drops from 3.80 to 3.23 eV when CeO_2 was doped with 4% of Ni and then rises for higher amount of doping; the authors attributed this change to the extensive structural changes caused by the incorporation of interstitial nickel. Whereby, in the current samples, with a Ni content of 3.66 wt%, a comparable doping level, that increases with the increase in the reduction temperature, can be assumed.

In order to highlight the nickel containing phases in the samples, the DR spectra were separated from the support contribution by subtraction of the related spectrum; the results are depicted in Fig. 2c. The calcined catalyst exhibited a weak band at around 370 nm that is usually ascribed to charge transfer of octahedral Ni^{2+} species in the free NiO lattices [64]; the weak intensity is probably due to the presence of small amount of NiO free on the surface, although inaccuracy in the subtraction method cannot be excluded. Since the NiO charge transfer band is generally revealed in the 250–350 nm range, the observed red shift indicates that less energy is necessary for charge transfer, as a result of interactions between Ni species and the La-Ce-Ox support, confirming previous evidences derived from the XRD [65]. In addition, a very intense band at 460 nm and the presence of a band at 720 nm suggests the presence of Ni^{2+} in octahedral position (Oh); whereas from the scarcely visible bands located at 535 and 648 nm, corresponding to Ni^{2+} in tetrahedral position (Th), the occurrence of a nickel spinels like phase can be established [66,67]. After reduction this nickel-species disappear although its presence, indicative of different degree of interaction with the support, can affect the reduction of the catalyst.

3.1.3. H_2 –temperature programmed reduction (TPR) and desorption (TPD) measurements

Fig. 3 shows H_2 -TPD traces of the catalyst after TPR, carried out to the reduction temperature of 450, 750 and 900 °C and maintaining the samples for 2 h to each temperature, this in order to quantify the type of Ni sites for hydrogen dissociation that can be formed during the pre-reduction of the sample. TPR of the catalyst, depicted in the inset of Fig. 3, shows a complex reduction profile characterized by the occurrence of multiple reduction peaks, located in

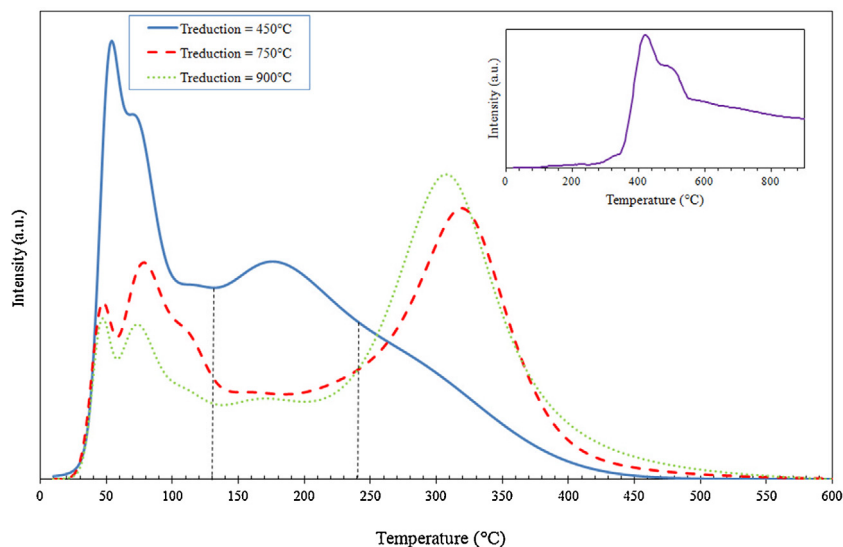


Fig. 3. H₂-TPD of the Ce_{0.70}La_{0.20}Ni_{0.10}O_{2-δ} catalyst pre-reduced at different temperature (Inset: TPR analysis).

Table 2

H₂ and CO chemisorption capability of the Ce_{0.70}La_{0.20}Ni_{0.10}O_{2-δ} sample reduced at different temperatures.

Sample	H ₂ chemisorption					CO chemisorption	
	σ ₁ ^a (μmol/g)	σ ₂ ^b (μmol/g)	σ ₃ ^c (μmol/g)	Ni surface (μmol/g)	Ni dispersion (%)	d _{Ni} (nm)	Ni dispersion (%)
T _{reduction} = 450 °C	8.9	7.5	5.0	23.2	6.8	14.2	0.92
T _{reduction} = 750 °C	5.4	3.3	9.7	9.3	2.9	33.0	0.63
T _{reduction} = 900 °C	3.8	3.1	11.2	6.9	2.0	48.5	0.47

^a amount of H₂ desorbed in the range between 25–140 °C.

^b amount of H₂ desorbed in the range between 140–240 °C.

^c amount of H₂ desorbed in the range between 240–600 °C.

the temperature range between 100 and 450 °C, and ascribed to different nickel species with different degree of interaction with the support: aggregated NiO particles dispersed on the surface (weak interaction) and crystalline bulk-like nickel phase (strong interaction), as previously evidenced [44]. A quantitative estimation of the Ni reduction peaks reveals a similar reduction degree, ranging between 51–56% by increasing the reduction's temperature, while obviously a noticeable increase in the ceria reduction can be observed (from 15 to 36%). Besides, on the basis of the current UV–vis studies, the presence of Ni²⁺_(Th), hardly reducible than the Ni²⁺_(Oh) species, hinders the reduction of the sample determining the low Ni reduction degree. As evident in Fig. 3, all the catalysts present a complex H₂ chemisorption region at low temperature (25–140 °C) associated with further desorption peaks evidenced at high temperatures, with the maximum located at 180 °C and 300–320 °C, respectively. The amount of H₂ desorbed, for the above-mentioned ranges of temperature, quantified as σ₁, σ₂ and σ₃, was derived after deconvolution of the recorded traces, the results are included in Table 2. It is evident from Fig. 3 that the desorption peaks are strongly influenced by the pre-reduction temperature, the peaks become broader and the maxima are shifted to higher temperature as the reduction temperature increases. The broadening of the low temperature peaks (σ₁ and σ₂ peaks) is associated with a progressive decrease in intensity by increasing the reduction temperature, while an opposite trend was observed for the σ₃ peak. This evidence indicates that new anchoring sites for H₂ spillover are formed by increasing the reduction temperature, in which the H₂ is more strongly retained; the population of this sites or the concentration increases by increasing the reduction temperature. The desorption in the low temperature region can be assigned to a weakly bound atomic hydrogen state on the surface of metallic Ni and/or in interaction with the surface oxygen

vacancies; while the σ₃ peak can be due to irreversibly adsorbed H states, in accordance with the literature [46,68]. The H₂ interaction with ceria is a mixture of bulk and surface events [69]; during the pre-reduction step the hydrogen atoms, derived from H₂-dissociation on Ni surface can migrate to the sub-surface layers and/or to the support (spillover effect) generating H-species, like bronze species (H_yCeO_{2-δ}), hydroxyl or hydride-type species, as previously described, whereby are revealed during TPD profiles at high temperature. The nickel dispersion was calculated from the total amount of the desorbed hydrogen up to 550 °C and supported by the evidence that in similar H₂-TPR/TPD experiments on the Ce_{0.78}La_{0.22}O_{2-δ} support the H₂ chemisorption was very low (0.83 μmol/g and 0.19 μmol/g after reduction at 450 and 900 °C, respectively) [46]. The derived values were 6.8, 2.9 and 2.0% providing an apparent Ni particle size of 14.2, 33.0 and 48.5 nm as result of the increased reduction temperature. The Ni particle size, related to the sample reduced at 450 °C, results in good agreement with as estimated from X-Ray line broadening, while higher values with the samples reduced at increasing temperature are derived. This evidence can suggest that the nickel crystallites are strongly bound to the support, with an interaction that increases by increasing the pretreatment temperature, and/or that the coverage of metal surface with the reduced support can occur; because the X-Ray broadening is not effected by surface poisoning and/or decoration effect whereby the estimated particle size result lower than derived from H₂ chemisorption [70]. As comparison, the CO pulse chemisorption was employed to determine the nickel dispersion; the results, included in Table 2, evidenced a very low dispersion that decreases progressively by increasing the pretreatment temperature and following the same trend previously derived from TPD. The gradual suppression of CO chemisorption, as well as H₂ chemisorption, after reduction at more severe conditions,

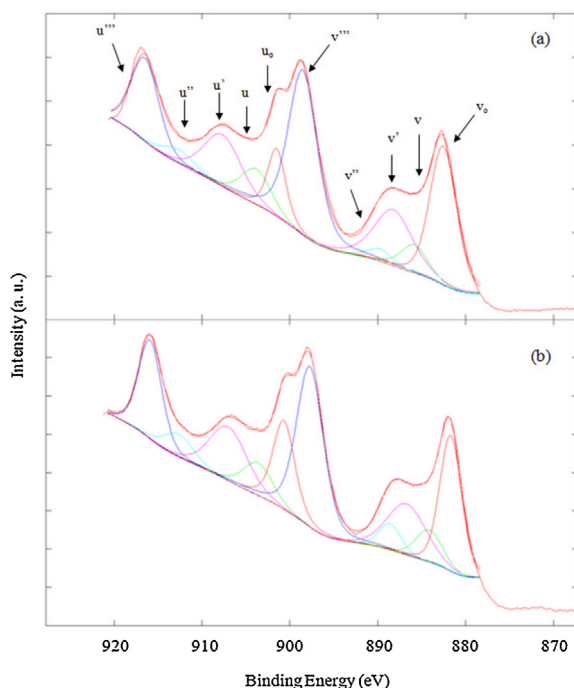


Fig. 4. Ce 3d XPS spectra of the $\text{Ce}_{0.70}\text{La}_{0.20}\text{Ni}_{0.10}\text{O}_{2-\delta}$ catalyst pre-reduced at 450 °C (a) and 900 °C (b), respectively.

can be due to the migration of partially reduced support species over the metallic particles, confirming the occurrence of an effect similar to the reported strong metal-support interaction (SMSI) [38–40]. Besides as only the exposed nickel metal atoms can be detected by chemisorption, whereas the nickel atoms at the metal-support interface are generally not measured, it is probable that this nickel species, in close proximity with anionic vacancies can be able to receive hydrogen in a hydride form, as previously discussed [49–51], whereby the dispersion from TPD results higher than the corresponding value derived from CO chemisorption.

3.1.4. XPS and SEM/EDX surface analysis over the reduced samples

XPS analyses were used to investigate the surface composition and the elements valence state of the more representative samples, reduced at 450 and 900 °C, respectively. The relevant atomic ratios as well as the binding energies (BE), from fitting of the main peaks related to O1s, Ni3p and $\text{La}3d_{5/2}$ core levels regions, are synthesized in Table 3. The Ni3p profiles, rather the more studied Ni2p profile, has been evaluated because the overlapping of $\text{Ni}2p_{3/2}$ and $\text{La}3d_{5/2}$ that may influence the accurate measure of BE and intensity of nickel. As previously observed [44], the binding energy for all peaks appears lower than the reference values, the shift appears more pronounced with the sample reduced at high temperature (900 °C); this evidence, discussed in sequence, results in accordance with the literature data on ceria mixed oxides whereby the BE are 0.7–1.0 eV lower than the single oxides [71]. Ce 3d XPS spectra are shown in Fig. 4; the deconvolution in the range of 880–925 eV, indexed to the two sets of peaks for both the Ce^{3+} and Ce^{4+} ionic states ($3d_{5/2}$, $3d_{3/2}$) labeled as v_0 , v , v_i , v_{ii} , v_{iii} and u_0 , u , u_i , u_{ii} , u_{iii} , respectively, confirms the presence of the mixed oxidation state of cerium. The concentration (%) of Ce^{3+} in the synthesized samples was calculated using the following equation:

$$\text{Ce}^{3+}, (\%) = \frac{u_0 + v_0 + v' + u'}{\sum (u + v)} \times 100 \quad (13)$$

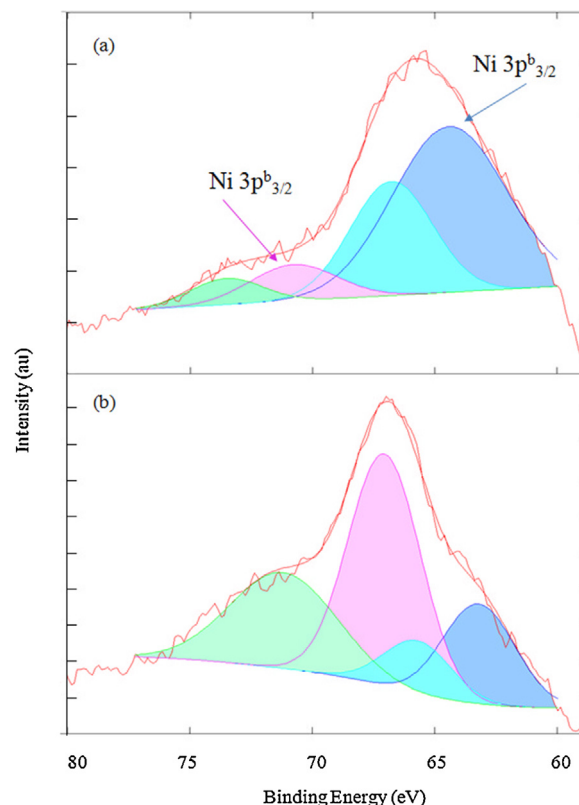


Fig. 5. Ni 3p XPS spectra of the $\text{Ce}_{0.70}\text{La}_{0.20}\text{Ni}_{0.10}\text{O}_{2-\delta}$ catalyst pre-reduced at 450 °C (a) and 900 °C (b), respectively.

As evidenced in Table 3, the relative concentration both in bulk and on surface increases by increasing the reduction temperature; the formation of oxygen vacancies that accompanies the change of the oxidation state of ceria, increases in parallel.

The O1s spectra can be resolved into three peaks corresponding to different oxygen species: the low binding energy peak at 526.4–527.6 eV can be ascribed to lattice oxygen ions (O^{2-}), the intermediate peak at 528.6–529.2 eV to adsorbed oxygen species (O^- , O^{2-}) and oxygen vacancies while the high energy band at 531.3 eV can be ascribed to hydroxyl and carbonate species (CO_3^{2-} , OH^-). The quantification of the corresponding proportion of each surface oxygen species is reported in Table 3; as evident the reduction at high temperature induces a noticeable loss of the lattice oxygen and a progressive increase in the population of the surface oxygen species. This can be explained considering that oxygen ions from the bulk can diffuse outwards and react with the hydrogen present in the surface layer to form hydroxyls, through a mechanism similar to that reported by Chung et al. [72] for TiO_2 reduced at 600 °C. The relative amount of surface-oxygen/lattice oxygen, estimated to be 3.5at% with the catalyst reduced at low temperature, that reaches 13at% after reduction at 900 °C, is strictly dependent by the change of oxidation state of the Ce ions from Ce^{4+} to Ce^{3+} which influences the concentration of partially reduced oxygen species and the content of vacancies defects. Intermediate values can be hypothesized for the sample reduced at 750 °C. Besides, a progressive decrease in the BE of $\text{La}3d_{5/2}$ by increasing the reduction temperature of the sample (reference value for $\text{La}^{3+}\text{La}_2\text{O}_3 = 834.8 \text{ eV}$ [73]) is observed, suggesting the partial reduction of La_2O_3 ; the resultant LaO_x ($x < 3$) species can act as electron donor, transferring electrons both to O^{2-} ions in the crystal lattice, leading to the shift of O species to lower binding energy, and similarly to the metallic Ni in close contact with La_2O_3 on the surface.

Table 3

Data from XPS analysis of the more representative pre-reduced catalysts.

Reduction Temperature (°C)	Binding Energy (eV)				Surface composition (at%)			Ce ³⁺ (at%)	
	Ni 3p ^a _{3/2}	Ni 3p ^b _{3/2}	O 1s	La 3d _{5/2}	Ni3p	La3d	Ce3d	In Ce	On surface
450	64.4 (2.35) ^o	68.0	527.6(22) [*] 529.2(43) [*] 531.3(34) [*]	833.81	1.5	3.3	8.2	47.6	3.9
900	64.1 (0.65) ^o	67.0	526.4 (7) [*] 528.6(69) [*] 531.3(22) [*]	833.07	2.5	2.9	8.9	47.9	4.3

* Relative amount (%) of the oxygen species calculated according to the area under the curves for each sub-peak.

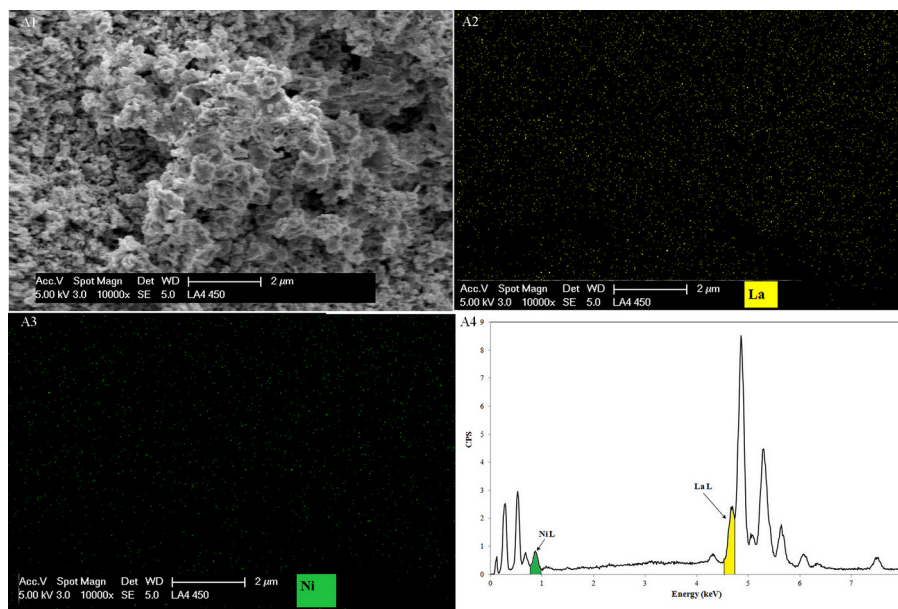
^o Values in parentheses are the area ratios corresponding to Ni 3p^a_{3/2} peak and Ni 3p^b_{3/2} peak.**Fig. 6.** SEM images (A1), La (A2) and Ni mapping (A3) with EDX spectrum (A4) of the Ce_{0.70}La_{0.20}Ni_{0.10}O_{2-δ} catalyst pre-reduced at 450 °C.

Fig. 5 shows the Ni 3p XPS spectra, the Ni3p_{3/2} and Ni3p_{1/2} contributions has been evaluated while the satellites from the Ni3p_{3/2} line are not included because they can hinder the separation between the Ni3p_{3/2}, p_{1/2} doublets [74]. The large value of the FWHM (full with half maximum) of Ni3p peak and its asymmetry on the high binding energy side suggests that both peaks might consists of more than one contribution. Thus, both lines were deconvoluted into two peaks, Ni3p^a_{3/2} and Ni3p^b_{3/2}, ascribed to metallic nickel and Ni²⁺ species, respectively; the results are evidenced in Table 3. The BE of Ni3p^a_{3/2}, assigned to metallic nickel, appears lower than the reference value (66.2 eV, [75]) in the catalyst reduced at 450 °C, and sensitively decreases to 64.1 eV increasing the reduction temperature; this suggests the occurrence of an electron transfer from La to Ni that increases by increasing the reduction's temperature. As consequence the d-electron density of the surface Ni atoms results increased and hence the Ni3p^a_{3/2} BE shifted toward lower values. As reported in Table 3, the area ratio of the Ni⁰/Ni²⁺ decreases progressively with the increasing the reduction temperature, indicating that the 70% of the surface Ni is in metal form carrying out the reduction at 450 °C then decreases to about 40% for the high reduction temperature. This evidence, in apparent contradiction with TPR results can be probably due to an overestimation of the reduction degree of Ni caused by the concurrent surface reduction of CeO₂ (happening generally at about 400 °C). Besides, it is interesting to note that the high reduction temperature induces a noticeable surface nickel enrichment associated with a decrease in the atomic concentration of La³⁺ ions indicat-

ing a greater dissolution of La³⁺ in the ceria lattice, in accordance with the increase in the lattice parameter observed during the XRD evaluations.

In order to confirm this evidence, the distribution of La and Ni in the near surface region has been evaluated by SEM/EDX analysis; the results as SEM images, EDX maps and profiles are reported in Figs. 6 and 7 for the samples reduced at 450 and 900 °C, respectively. As evident La and Ni appear uniformly distributed on the surface region in both samples; the large dot intensity of La, evidenced in some regions of the sample reduced at low temperature (Fig. 6-A2), that decrease after reduction at high temperature, can suggest the La redistribution and/or migration to the sub-layers of the catalyst (Fig. 7-B2). Opposite behavior can be envisaged by Ni; besides EDX spectra (Figs. 6-A4 and 7-B4) show a progressive increase in the Ni signal by increasing the reduction temperature suggesting a partial nickel exsolution from the bulk. The high presence of surface oxygen species can oxidize this nickel particles, whereby the observed Ni⁰/Ni²⁺ ratio on surface decreases, as previously derived from XPS, and/or a higher concentration of surface Ni solid solution can be formed.

Recent studies on perovskite oxides (ABO₃), carried out by the J.T.S. Irvine's group, have highlighted as the high concentration of oxygen vacancies, induced by H₂ reduction, leads the metal exsolution from the B-site in the perovskite matrices when the composition is altered to A/B < 1 to re-establish the stoichiometry [76,77]. In La_{0.4}Sr_{0.4}Ni_{0.03}Ti_{0.93}O_{3-γ} sample, after H₂ reduction at 900 °C for 20 h, the Author showed that nickel diffuses from

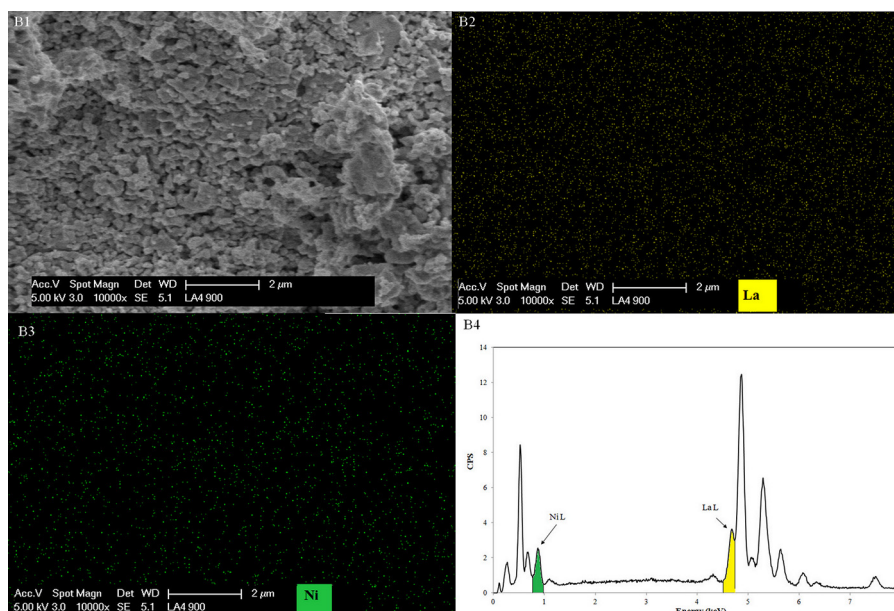


Fig. 7. SEM images (B1), La (B2) and Ni mapping (B3) with EDX spectrum (B4) of the $\text{Ce}_{0.70}\text{La}_{0.20}\text{Ni}_{0.10}\text{O}_{2-\delta}$ catalyst pre-reduced at 900 °C.

the bulk to the surface forming metallic particles, while La^{3+} fills the surface A-site vacancies [77]. Qi et al. [78] in Ni/CeO_2 electrocatalysts, reduced at 1200 °C for 6 h, evidenced the exsolution of metallic nickel associated with the presence of Ni^{2+} nanoparticles; the authors ascribed the partial oxidation of the metal to the adsorption of atmospheric oxygen on the surface or to the formation of superficial solid solution. Analogous behavior can be involved in the current samples induced by the high H_2 -reduction temperature.

3.2. Catalytic performance studies

Fig. 8 show the effect of the GHSV on the catalytic performance, as CH_4/CO_2 conversion and H_2/CO molar ratio in the product stream, versus time on stream over the pre-reduced catalysts. The sample reduced at 450 °C shows at the lowest GHSV (26400 h^{-1}) an initial CH_4 conversion of 86%, equal to the equilibrium conversion of methane at 750 °C. A rapid decline in the catalytic activity along the first 5 h of reaction can be observed, then the CH_4 conversion remain stable for the successive 45 h of reaction. The CO_2 conversion, following the same trend, remains higher than the CH_4 conversion; this is mainly due to the occurrence of the reverse water gas shift reaction (RWGS : $\text{CO}_2 + \text{H}_2 \leftrightarrow \text{H}_2\text{O} + \text{CO}$), as emerges from the presence of H_2O as by-product of the reaction and from the related H_2/CO molar ratio lower than the unit, as evidenced in Fig. 8b. The decline in the activity appears more evident by increasing the GHSV, a loss of the CH_4 conversion of about 21% along 50 h of the time on stream was revealed at a GHSV of 52800 h^{-1} ; while, a higher gas hourly space velocity (105600 h^{-1}) the decay in the CH_4 conversion during the initial 40 h of reaction reaches a value of 68%, then the activity remains stable for further 10 h. This initial period of activation, strongly influenced by the GHSV, can be due to the possible changes in the surface structure of the catalyst to a more stable form under the reaction ambient.

The pre-reduction of the catalyst at 750 °C induces a decrease in the initial CH_4 conversion, 72% at $\text{GHSV} = 26400 \text{ h}^{-1}$ and 65% at $\text{GHSV} = 52800 \text{ h}^{-1}$, that remains invariant during the 50 h of the reaction; while, increasing the gas hourly space velocity, the low initial conversion (55%) progressively decreases during the time on stream with a decay in the conversion of about 16%. A slight decrease in the initial performance with the catalyst reduced at

900 °C was observed, the sample results stable during the test at the lowest GHSV; while, an increase in the decay by increasing the gas hourly space velocity was evidenced.

In order to verify if the observed catalytic behavior can be ascribed to carbon deposition, one of the main causes of the catalyst decay during dry reforming reaction, temperature programmed oxidation (TPO) on spent catalysts was performed, examining both nature and coking formation rates of the carbon species present. TPO-MS profiles, including the CO_2 signal ($m/z = 44_{\text{CO}_2}$) of the catalyst, pre-reduced at 450 °C and tested at increasing GHSV, are shown in Fig. 9. A large and asymmetric peak at 670 °C with a shoulder at about 580 °C, with intensity that increases by increasing the GHSV was observed. This peak can be attributed to the gasification of filamentous carbon with different diameters; fibers with smaller diameter can be oxidized easily than those with larger diameter, thus the oxidation occurs at low temperature, this produces the peak broadening at low temperature [79]. Negligible CO_2 traces was revealed over the spent catalysts pre-reduced at high temperatures also after the tests at high GHSV, as evidenced in the inset of Fig. 9. The derived carbon formation rate, reported in Table 4, increases slightly by increasing the GHSV and appears independent from the reduction temperature of the catalyst. This can be related to a more oxidative atmosphere generated by increasing the GHSV, due to the low conversion, that accelerates the deactivation and can induce the Ni re-oxidation. The related amount of deposited carbon on the catalyst pre-reduced at 450 °C increases from 21.6 to 27.2% by increasing the GHSV; while, a very low coking rate and exiguous amount of deposited carbon was observed with the samples pre-reduced at 750 and 900 °C, respectively. Fig. 10a shows the post-reaction SEM image of the catalyst pre-reduced at 450 °C and tested at high GHSV (105600 h^{-1}), the presence of large amount of filamentous carbon, with diameter ranging between 0.02–0.1 μm , can be observed. This confirms previous TPO observations; absence of carbon deposition on the remaining samples emerges, as evidenced in Fig. 10b and c.

Although the initial activity of the catalyst reduced at 450 °C was similar during the tests at different GHSV, the deactivation appears due to the carbon deposition, as emerges from TPO analysis; while the catalysts reduced at 750 °C and 900 °C shown an initial activity lower than that derived with previous sample but more stable and associated with a very low carbon deposition also during the tests

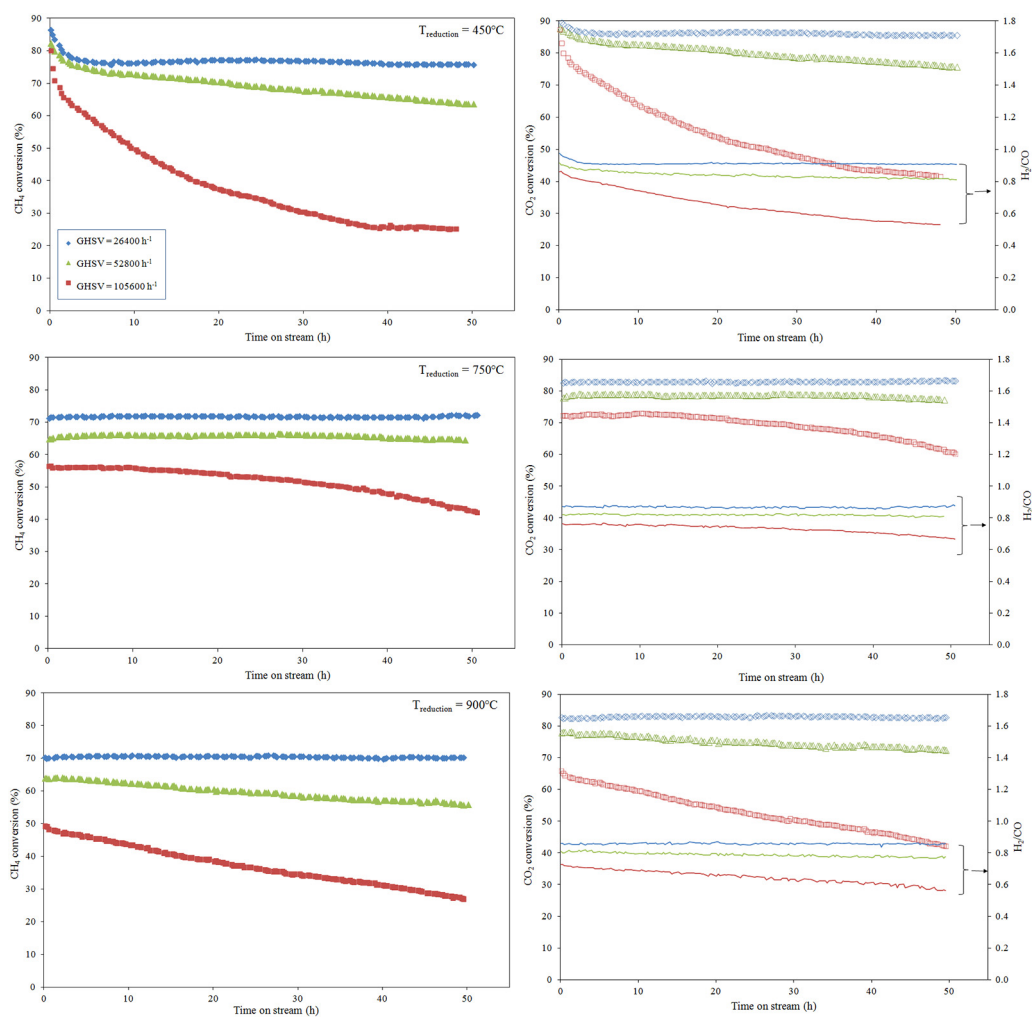


Fig. 8. Effect of the pre-reduction temperature at increasing GHSV (26400–105600 h⁻¹) on CH₄, CO₂ conversion and H₂/CO molar ratio during methane dry reforming carried out at 750 °C.

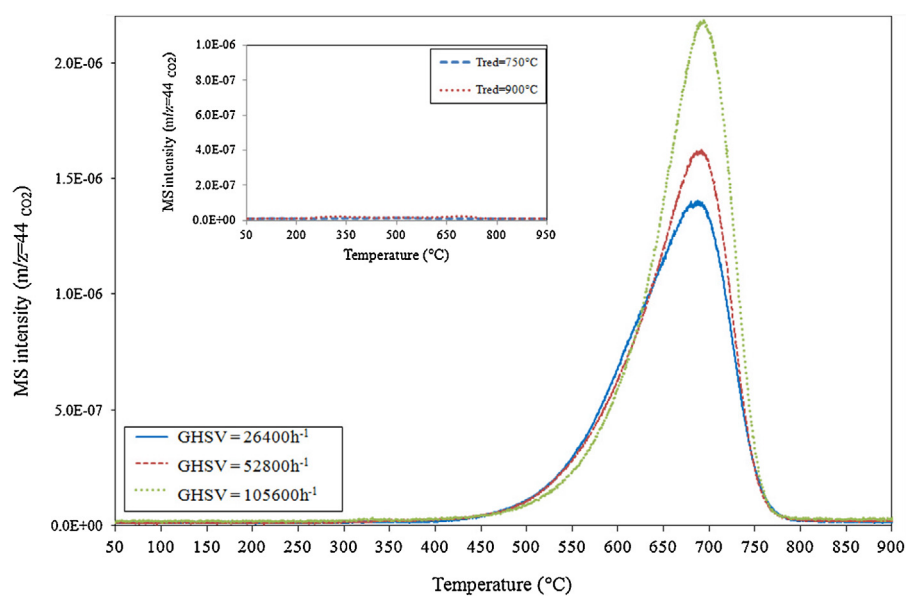
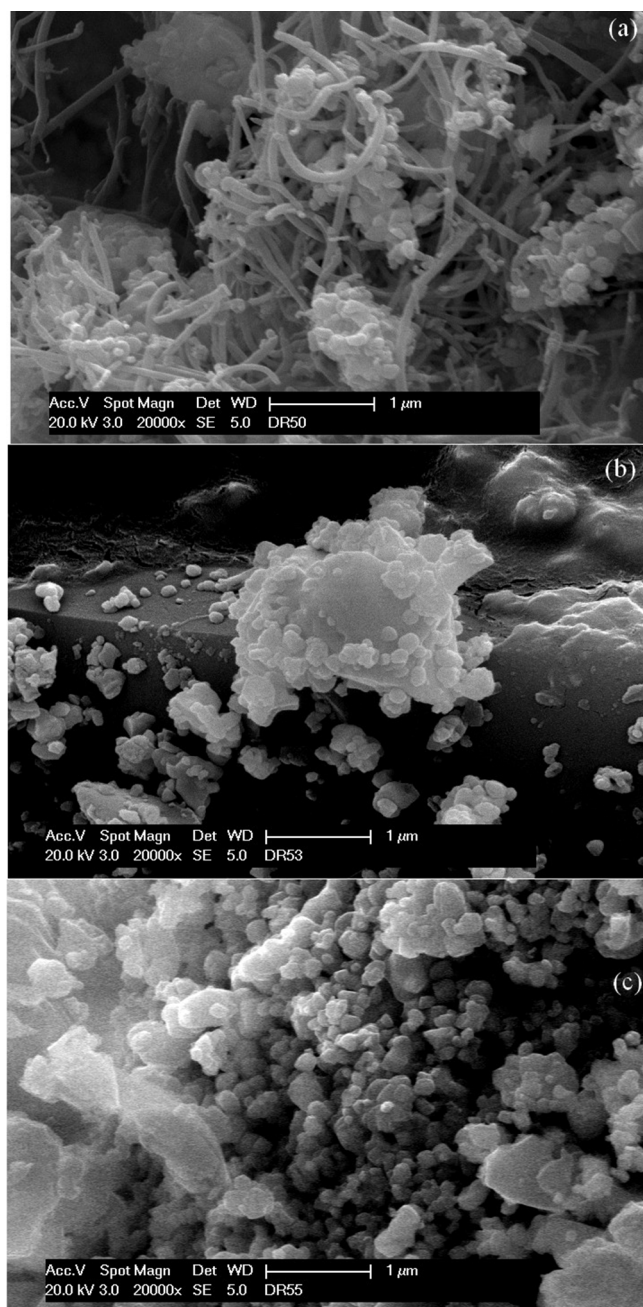


Fig. 9. MS signal ($m/z = 44_{\text{CO}_2}$) during TPO tests over the spent catalysts pre-reduced at 450 °C tested at increasing GHSV. Insert: Magnification of the analogous characterization test over the spent samples pre-reduced at 750 and 900 °C after dry reforming reaction at GHSV = 105600 h⁻¹.

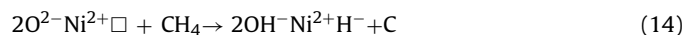
Table 4

Catalytic activity after 50 h of reaction, deactivation rate, carbon deposition after TPO experiments and apparent turnover frequency (TOF).

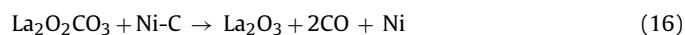
Reduction temperature (°C)	GHSV (h ⁻¹)	Carbon formation rate (mg/g _{catalyst} ·h)	Deposited carbon (%)	TOF (s ⁻¹)
450	26400	4.33	21.6	2.0
450	52800	4.65	23.2	3.8
450	105600	5.45	27.2	7.5
750	26400	0	0	4.2
750	52800	0.02	0.12	7.6
750	105600	0.04	0.20	12.9
900	26400	0.08	0.36	5.5
900	52800	0.11	0.55	10.1
900	105600	0.12	0.59	15.6

**Fig. 10.** SEM images of the spent catalysts, pre-reduced at increasing temperature (a: 450 °C; b: 750 °C and c: 900 °C), after the catalytic activity carried out at GHSV = 105600 h⁻¹.

at high GHSV (Table 4). The decline in the initial activity by increasing the reduction temperature can be related to more factors like the increase in the Ni particle size, as revealed from XRD, or to the decrease in the metal dispersion, as evidenced in Table 2, and to the reduced presence of metallic nickel, as derived from XPS. The very low amount of carbon deposition may be indicative of changes in the metal support-interactions induced by H₂-pretreatment, that contribute to the balance of the reaction rates inducing carbon formation and removal. It is widely accepted that the dry reforming reaction proceeds on metallic nickel that activates CH₄, producing CH_x and H₂; whereas, the CO₂ adsorbed on support dissociates producing adsorbed oxygen and gaseous CO. The presence of oxygen vacancies on the support can further speed the reaction of CH_x with oxygen coming from CO₂, speeding up the CO₂ activation and dissociation. XPS investigations have highlighted as the increase in the temperature of H₂ pretreatment determines a progressive increase in surface Ni²⁺, and in the concentration of oxygen vacancies. Ni²⁺ species, present in the solid solution lanthana-ceria and/or at the interface Ni-solid solution can help the abstraction of hydrogen species from CH₄ involving the anionic vacancies, as follows:

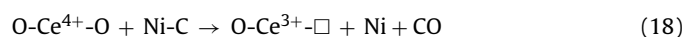


due to the ability of the solid to accept hydrogen, forming carbon. It is probable that after reduction at high temperature ($T \geq 750^\circ\text{C}$) the high d-electron density of the surface Ni atoms can inhibit the donation of the electron pair of C–H bond from CH₄ to the unfilled d-orbital of nickel, whereby the CH₄ dehydrogenation to carbon decreases sensitively. While, donation of the d-electron of the nickel atoms to anti-bonding π^* orbit of CO₂ molecules can occur, activating the CO₂, that can promote the carbon elimination. Besides the CO₂, reversibly adsorbed on the surface La₂O₃, generates carbonate species at the boundary of Ni particles that, reacting with the deposited carbon forms CO:



regenerating the active sites, again available for CO₂ and CH₄ activation.

Finally, the presence of oxygen vacancies can promote the CO₂ dissociation, the formed lattice oxygen diffuses towards the Ni surface and reacts with the carbon formed by CH₄ decomposition, in accordance with the following steps [32]:



while, the large concentration of labile oxygen can further promote the carbon removal to CO and/or CO₂. All this combined effects can minimize the carbon deposition.

The activity of the current catalytic system appears very promising if compared with the performance of catalysts reported in literature, as shown below. Gonzalez-Delacruz et al. [80], with

13wt%Ni/CeO₂ catalyst prepared also by combustion synthesis, evidenced during dry reforming reaction carried out at 750 °C under a GHSV of 3 10⁵ L/kg h high CH₄ conversion (90%) but severe carbon deposition. Ni/CeO₂ nanorods, synthesized by hydrothermal method, showed a CH₄ conversion of 85% and a CO₂ conversion of 90% that decrease by 21.9% and 12.1%, respectively, along 30 h of reforming tests carried out at 700 °C and GHSV of 18000 ml/h g. The observed decay in the catalytic performance was due to carbon nanotubes formation [31]. Dacquin et al. [81] adopted the “in situ crystallization in confined space” procedure to prepare Ni/lanthanum-doped mesoporous composite (SBA10). High stability of the sample during reaction, carried out at 700 °C under a GHSV of 600L/g h was derived. The catalytic system reaches 75% CH₄ conversion and 85% CO₂ conversion, respectively, associated with carbon filaments accumulation during 48 h of reaction. The investigations of Kambolis et al. [29], on 5wt%Ni supported on binary CeO₂-ZrO₂ supports (20–100 CeO₂ molar ratio), evidenced that the sample rich in zirconium exhibited higher activity and strong resistance to carbon formation than that supported on pure ceria. Recently Makri et al. [32] evaluated the effect of Pr³⁺ and Zr⁴⁺ as dopants in 5wt%Ni/CeO₂; from the reported study emerges a high stability of 5wt%Ni/Ce_{0.8}Pr_{0.2}O₂ catalyst, evidenced by a CO₂ conversion of 84% (CH₄conv.=78%) after 50 h of reaction at 750 °C (GHSV = 30000 h⁻¹). Accumulation of relatively low “inactive” carbon (1.75 wt%) was observed. The beneficial effect of trivalent cations on the activity of ceria-based catalyst is evidenced also with noble metal catalysts; F. Wang et al. [82] obtained superior performance of Ir/Ce_{0.9}La_{0.1}O₂ sample than the corresponding Ir/CeO₂ during dry reforming at 750 °C along a wide range of GHSV (5000–36000 ml/g h). Stability tests, with Ir/CeO₂ sample under a GHSV of 18000 ml/g h showed a slight decrease of the CH₄ conversion from 54 to 45% after 200 h of time on stream; while Ir/Ce_{0.9}La_{0.1}O₂ sample maintains stable performance CH₄conv = 60%; CO₂conv = 70% also at high GHSV (36000 ml/g h) for long time (1000 h) with very low amount of carbon deposition (0.6 wt%).

In order to clarify the complex effect of the pre-reduction temperature on the physico-chemical properties and the consequently relation with the catalytic activity and stability of the samples, the apparent turnover frequency (TOF), have been derived. The initial CH₄ conversion (10 min), considering the dissociative adsorption of methane as rate determining step, and the number of available Ni surface atoms, from TPD studies, has been used. Although high conversion level was not reliable, this was done only to compare the intrinsic activity of the species formed under the reduction treatment of the catalyst with the catalytic activity, the results are included in Table 4. As evident, the TOF values increases by increasing the reduction temperature of the catalyst, the GHSV and the apparent size of Ni particles, this is depicted in Fig. 11a. The increase in TOF by increasing the Ni particle size results in apparent contradiction with theoretical and experimental evidences that demonstrate as the TOF values decrease by increasing the particle size of the supported metal [45,83,84]. Zhang et al. [85] showed that the TOF values decrease with the increase in the Rh particle size supported on Al₂O₃ and TiO₂; analogous trend has been observed by Wang et al. [86] on mesoporous Ni-Ce-Al oxides. This behavior is primarily due to the prevalence of coordinatively unsaturated metal surface atoms in smaller clusters that can effectively activate C–H bonds more than atoms on lower-index surfaces [87].

In addition, the apparent TOF has been plotted as a function of the fraction of σ₃ sites (Fig. 11b), derived from the fractional area of the high temperature desorption peak revealed during TPD. The TOF increases by increasing the fraction of this sites; this suggests that the reduction at high temperature induces changes in the morphology of nickel particles due to the interaction with the reduced ceria, probably increasing the content of step and kink

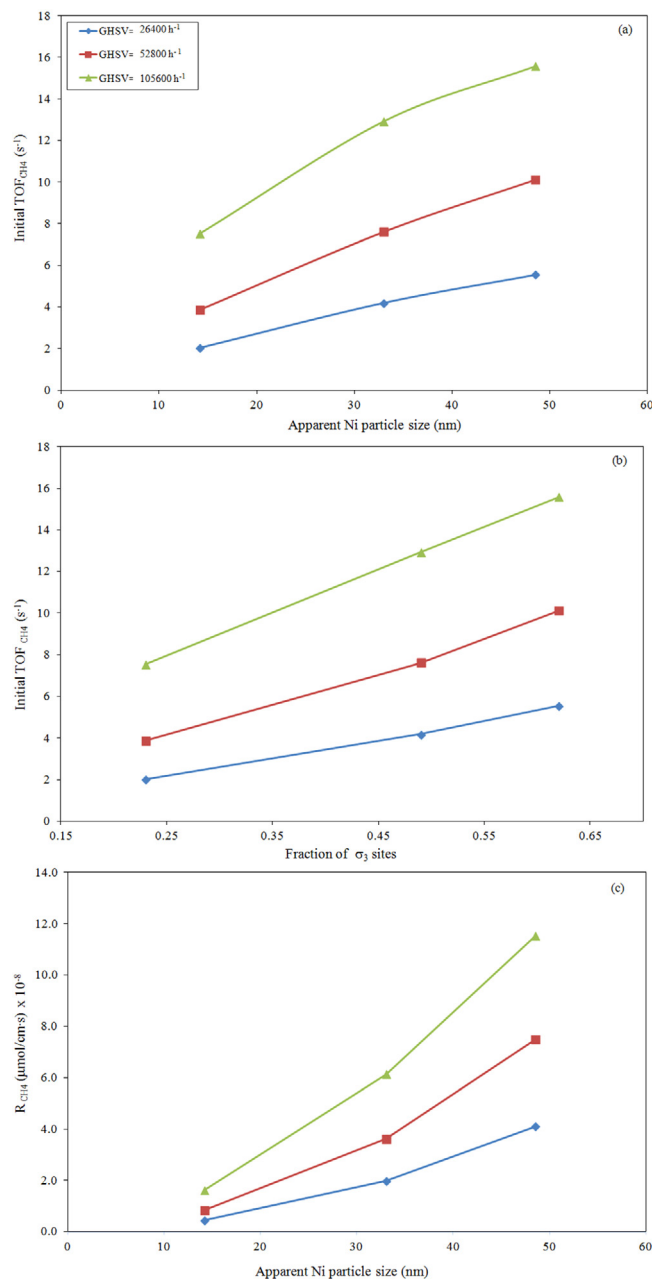


Fig. 11. Initial TOF_{CH₄} versus apparent Ni particle size (a) and fraction of σ₃ sites for methane dry reforming reaction carried out at 750 °C under different GHSV compared with the specific activity (R_{CH₄}) calculated according to the concentration of interfacial perimeter Ni-support.

sites, very active for methane dry reforming. Recent studies of Gonzales-Delacruz et al. [38] have demonstrated, from in situ XAS and APPES spectroscopy, as the H₂-reduction at 750 °C of Ni/CeO₂ catalyst causes a decrease in the coordination number of metallic particles spreading the particles on partially reduced support. These flattened particles with low unsaturated metal sites result very stable during dry reforming reaction. In the current samples the pre-reduction at increasing temperature induces, as evidences by XPS, increasing interactions Ni-support that in turn progressively may influence the availability of sites (step and kink) with high reactivity both to the dissociative adsorption of CH₄, but also the carbon diffusion into the nickel lattice. At low reduction temperature (450 °C) the low interactions determine a high availability of unsaturated Ni atoms that contribute to the high catalytic activity and carbon deposition. Increasing the reduction temperature,

this interactions progressively increase and the concentration of unsaturated Ni atoms probably decreases determining the lower catalytic activity but absence of carbon deposition. This effect may be responsible of the stability, reached by the sample pretreated at 450 °C, during the reaction at high time on stream (Fig. 8) due to the interactions with the produced H₂ at the reaction temperature (750 °C).

Besides, in the current catalyst the presence of La₂O₃ can suggest a bi-functional mechanism where, the CH₄ activation on the Ni surface, is not the only rate determining but also the reaction of oxy-carbonate species at the boundary of the Ni particles (eq. 16) can be considered a slow step, in accordance with previous evidences reported by Verykios's group, on Ni/La₂O₃ catalyst [88,89], and more recently by Sokolov et al. [90] during methane dry reforming with Ni-La₂O₃-ZrO₂ catalysts. On this basis, it is likely that the interfacial atoms are involved in the reaction mechanism; a more quantitative evaluation of the metal/support interface can be provided by an estimation of the interfacial perimeter between Ni particles and support. The length of the perimeter Ni-support interface (l_0 , cm/g) was derived by application of the following equation, reported by Duprez and coworkers [91,92]:

$$l_0 = \beta D_0^2 x_m \quad (19)$$

where β (6.37 10⁵ m/g) is a shape factor based on the interfacial perimeter of cubic Ni particles over the support surface; D_0 is the Ni dispersion and x_m the nickel content. The specific activity calculated on the length of the derived peripheral interface nickel-support, reported as R_{CH_4} (μmol/cm s), is plotted in Fig. 11c; as evident the R_{CH_4} noticeable increases by increasing the apparent Ni particles size, appearing due to a decrease in the l_0 value (from 1.08 10¹⁰ to 9.3 10⁸ cm/g) by increasing the reduction temperature. Kalamaras et al. [46], studying the water gas shift reaction with Pt/CeO₂ catalyst, observed analogous linear trend between specific kinetic rate (estimated on the periphery of Pt/CeO₂ interface) and Pt particle size. The observed behavior was ascribed to the different local electron density, depending from the Pt particle size, that influences the reactivity of oxygen atoms of the support. It is likely that in the current samples the changes in the coordination number and density of Ni sites along the metal-support interface, induced by the H₂-treatment determines the observed trend. So, although the interfacial perimeter decreases by increasing the reduction temperature, the morphological change in nickel particles induced by H₂ treatment can influence the catalyst reactivity. Detailed kinetic investigations, in progress, will further clarify this aspect.

4. Conclusion

This preliminary studies evidences as the Ce_{0.70}La_{0.20}Ni_{0.10}O_{2-δ} sample is a promising catalytic system for biogas (methane) dry reforming reaction, carried out at 750 °C, with appreciable resistance to carbon deposition. Absence of carbon deposition was revealed at a GHSV of 26400 h⁻¹; while, negligible amount (0.12–0.20%) was deposited also at increasing GHSV (52800–105600 h⁻¹) after H₂ pre-reduction of the catalyst at 750 °C.

Characterizations of the catalyst reveal strong Ni-support interactions, or solid-solution formation, that increase by increasing the pre-reduction temperature of the sample (from 450 to 900 °C); XPS revealed an high reduction degree of Ni (70%) after reduction at 450 °C, that decreases after H₂-pretreatment at high temperature (900 °C) with surface enrichment of Ni²⁺ on the surface. A good balance between Ni reduction degree and metal-support interactions, probably occurring after reduction at 750 °C, can be responsible of the high resistance to carbon deposition observed.

The apparent specific activity, TOF_{CH₄} (s⁻¹) and/or R_{CH_4} (μmol/cm s) based on the exposed Ni atoms and Ni-support interface respectively, increases by increasing the nickel particles size this can be rationalized by a double assumption: a) the reduction at increasing temperature modify the morphology of nickel particles; b) bi-functional mechanism can be predicted, where not only the methane decomposition but also the removal of carbon deposition by interfacial sites Ni-La₂O₃ can be considered rate determining step of the reaction.

References

- [1] IPCC, Climate change 2014: synthesis report, in: R.K. Pachauri, L.A. Meyer (Eds.), Contribution of Working Groups I, II and III to the Fifth Assessment Report of the Intergovernmental Panel on Climate Change [Core Writing Team, IPCC, Geneva Switzerland, 2014, 151 pp.
- [2] X.F. Lou, J. Nair, Bioresour. Technol. 100 (2009) 3792–3798.
- [3] A.P.E. York, T.-C. Xiao, M.L.H. Green, J.B. Claridge, Catal. Rev. 49 (2007) 511–560.
- [4] Y.H. Hu, E. Ruckenstein, Adv. Catal. 48 (2004) 297–345.
- [5] T.V. Choudhary, V.R. Choudhary, Angew. Chemie. 47 (2008) 1828–1847.
- [6] K. Wang, X. Li, S. Ji, B. Huang, C. Li, Chem. Sust. Chem. 1 (2008) 527–533.
- [7] D. Fraenkel, R. Levitan, M. Levy, Int. J. Hydrogen Energy 11 (1986) 267–277.
- [8] M. Levy, R. Levitan, Sol. Energy 50 (1993) 1978–1989.
- [9] S. Wang, G.Q. Lu, Energy Fuels 10 (1996) 896–904.
- [10] D. Pakhare, J. Spivey, Chem. Soc. Rev. 43 (2014) 7813–7837.
- [11] Z. Hou, T. Yashima, Appl. Catal. A 261 (2004) 205–209.
- [12] J.B. Claridge, M.L.H. Green, S.C. Tsang, A.P.E. York, A.T. Ashcroft, P.D. Battle, Catal. Lett. 22 (1993) 299–305.
- [13] M.A. Goula, A.A. Lemonidou, A.M. Efstathiou, J. Catal. 161 (1996) 626–640.
- [14] D. Chen, R. Lodeng, A. Anundskas, O. Olsvik, A. Holmen, Chem. Eng. Sci. 56 (2001) 1371–1379.
- [15] V.C.H. Kroll, H.M. Swaan, S. Lacombe, C. Mirodatos, J. Catal. 164 (1996) 378–398.
- [16] Z.X. Cheng, X.G. Zhao, J.L. Li, Q.M. Zhu, Appl. Catal. A 205 (2001) 31–36.
- [17] A.F. Lucrédio, J.M. Assaf, E.M. Assaf, Appl. Catal. A 400 (2011) 156–165.
- [18] A. Serrano-Lotina, A.J. Martin, M.A. Folgado, L. Daza, Int. J. Hydrogen Energy 37 (2012) 12342–12350.
- [19] J. Chen, R. Wang, J. Zhang, F. He, S. Han, J. Mol. Catal. A: Chem. 235 (2005) 302–310.
- [20] T. Odedairo, J. Chen, Z. Zhu, Catal. Comm. 31 (2013) 25–31.
- [21] J.-M. Wei, B.-Q. Xu, J.-L. Li, Z.-X. Cheng, Q.-M. Zhu, Appl. Catal. A 196 (2000) 1167–1172.
- [22] L. Li, B.S. Liu, J.W.H. Leung, C.T. Au, A.S.-C. Cheung, Catal. Today 131 (2008) 533–540.
- [23] X. Zhu, P. Huo, Y.-P. Zhang, D.-G. Cheng, C.-J. Liu, Appl. Catal. B 81 (2008) 132–140.
- [24] A.E. Castro Luna, M.E. Iriarte, Appl. Catal. A 343 (2008) 10–15.
- [25] J.-S. Choi, K.-I. Moon, Y.G. Kima, J.S. Lee, C.-H. Kimb, D.L. Trimm, Catal. Lett. 52 (1998) 43–47.
- [26] K.Y. Koo, H.-S. Roh, Y.T. Seo, D.J. Seo, W.L. Yoon, S.B. Park, Appl. Catal. A 340 (2008) 183–190.
- [27] H. Xiao, Z. Liu, X. Zhou, K. Zhu, Catal. Comm. 34 (2013) 11–15.
- [28] P. Djinić, I.G. Osojnik Črnivec, B. Erjavec, A. Pintar, Appl. Catal. 125 (8) (2012) 259–270.
- [29] A. Kambolis, H. Matralis, A. Trovarelli, Ch. Papadopoulou, Appl. Catal. A 377 (2010) 16–26.
- [30] F. Ocampo, B. Louis, L. Kiwi-Minsker, A.-C. Roger, Appl. Catal. A 392 (2011) 36–44.
- [31] X. Du, D. Zhang, L. Shi, R. Gao, J. Zhang, J. Phys. Chem. C 116 (2012) 10009–10016.
- [32] M.M. Makri, M.A. Vasiliades, K.C. Petalidou, A.M. Efstathiou, Catal. Today 259 (2015) 150–164.
- [33] S.J. Tauster, S.C. Fung, R.L. Garten, J. Am. Chem. Soc. 100 (1978) 170–175.
- [34] S.E. Golunski, H.A. Hatcher, R.R. Rajaram, T.J. Truex, Appl. Catal. B: Environ. 5 (1995) 367–376.
- [35] S. Bernal, J.J. Calvino, M.A. Cauqui, J.M. Gattica, C. Lopez-Cartles, J.A. Perez Omil, J.M. Pintado, Catal. Today 77 (2003) 385–406.
- [36] A.K. Dayte, D. Kalakkad, M.H. Yao, D.J. Smith, J. Catal. 155 (1995) 148–153.
- [37] K. Schierbaum, Surf. Sci. 399 (1998) 29–38.
- [38] V.M. Gonzalez-Delacruz, J.P. Holgado, R. Pereñíguez, A. Caballero, J. Catal. 257 (2008) 307–314.
- [39] A. Caballero, J.P. Holgado, V.M. Gonzalez-delaCruz, S.E. Habas, T. Herranz, M. Salmeron, Chem. Comm. 46 (2010) 1097–1099.
- [40] X. Du, D. Zhang, L. Shi, R. Gao, J. Zhang, J. Phys. Chem. C 116 (2012) 10009–10016.
- [41] Y. Zhou, J. Zhou, J. Phys. Chem. C 116 (2012) 9544–9549.
- [42] J. Carrasco, L. Barrio, P. Liu, J.A. Rodriguez, M.V. Ganduglia-Pirovano, J. Phys. Chem. C 117 (2013) 8241–8250.
- [43] A. Kubacka, A. Martínez-Arias, M. Fernández-García, ChemCatChem 7 (2015) 3614–3624.
- [44] L. Pino, A. Vita, M. Laganà, V. Recupero, Appl. Catal. B 148–149 (2014) 91–105.

- [45] Y.-H. Wang, H.-M. Liua, B.-Q. Xu, *J. Mol. Catal. A* 299 (2009) 44–52.
- [46] C.M. Kalamaras, S. Americanou, A.M. Efstathiou, *J. Catalysis* 279 (2011) 287–300.
- [47] T. Takeguchi, S. Manabe, R. Kikuchi, K. Eguchi, T. Kanazawa, S. Matsumoto, W. Ueda, *Appl. Catal. A* 293 (2005) 91–96.
- [48] S.J. Hong, A.V. Virkar, *J. Am. Ceram. Soc.* 78 (1995) 433–439.
- [49] C. Lamonier, A. Ponchel, A. D'Huysser, L. Jalowiecki-Duhamel, *Catal. Today* 50 (1999) 247–259.
- [50] L. Jalowiecki-Duhamel, A. Ponchel, C. Lamonier, *Int. J. Hydrogen Energy* 24 (1999) 1083–1092.
- [51] L. Jalowiecki-Duhamel, J. Carpentier, A. Ponchel, *Int. J. Hydrogen Energy* 32 (2007) 2439–2444.
- [52] A. Bensalem, J.C. Muller, F. Bozon-Verduraz, *J. Chem. Soc. Faraday Trans.* 88 (1992) 153–154.
- [53] M.I. Zaki, G.A.M. Hussein, S.A.A. Mansour, H.M. Ismail, G.A.H. Mekhemer, *Colloid Surf. A* 127 (1997) 47–56.
- [54] M.A. Centeno, C. Portales, I. Carrizosa, J.A. Odriozola, *Catal. Lett.* 102 (2005) 289–297.
- [55] W. Lee, S.-Y. Chen, E. Tseng, A. Gloter, C.-L. Chen, *J. Phys. Chem. C* 120 (2016) 14874–14882.
- [56] L. Katta, P. Sudarsanam, G. Thrimurthulu, B.M. Reddy, *Appl. Catal. B: Environ.* 101 (2010) 101–108.
- [57] L. Katta, G. Thrimurthulu, B.M. Reddy, M. Muhler, W. Grünert, *Catal. Sci. Technol.* 1 (2011) 1645–1652.
- [58] R.J.M. Mattos, S.H. Probst, J.C. Afonso, M. Schmal, *J. Braz. Chem. Soc.* 15 (2004) 760–766.
- [59] K.C. Petallidou, A.M. Efstathiou, *Appl. Catal. B: Environ.* 140–141 (2013) 333–347.
- [60] C. Sun, H. Li, H. Zhang, Z. Wang, L. Chen, *Nanotechnology* 16 (2005) 1454–1463.
- [61] X. Lu, X. Li, F. Chen, C. Ni, Z. Chen, *J. Alloys Compd.* 476 (2009) 958–962.
- [62] S. Kumar, A.K. Ojha, *RSC Adv.* 6 (2016) 8651–8660.
- [63] A. Thurber, K.M. Reddy, V. Shutthanandan, M.H. Engelhard, C. Wang, J. Hays, A. Punnoose, *Phys. Rev. B* 76 (2007), 165206/1–165206/8.
- [64] B. Li, X. Xu, S. Zhang, *Int. J. Hydrogen Energy* 38 (2013) 890–900.
- [65] J. da, S. Lisboa, D.C.R.M. Santos, F.B. Passos, F.B. Noronha, *Catal. Today* 101 (2005) 15–21.
- [66] E. Kis R. Marinkovic, G. Lomic, D.Z. Boskovic, J. Obadović, J. Kiurski, P. Putanov, *Polyhedron* 17 (1998) 27–34.
- [67] M. Lo Jacono, M. Schiavello, A. Cimino, *J. Phys. Chem.* 76 (1971) 1044–1050.
- [68] X. Liao, Y. Zhang, M. Hill, X. Xia, Y. Zhao, Z. Jiang, *Appl. Catal. A: Gen.* 488 (2014) 256–264.
- [69] A. Laachir, V. Perrichon, A. Badri, J. Lamotte, E. Catherine, J.C. Lavalley, J. El Fallah, L. Hilaire, F. Le Normand, E. Quéméré, G.N. Sauvion, O. Touret, *J. Chem. Soc. Faraday Trans.* 87 (1991) 1601–1609.
- [70] N.A. Pechimuthu, K.K. Pant, S.C. Dhingra, R. Bhalla, *Ind. Eng. Chem. Res.* 45 (2006) 7435–7443.
- [71] A. Galtayries, R. Sporken, J. Riga, G. Blanchard, R. Caudano, *J. Electron Spectrosc. Rel. Phenom.* 88–91 (1998) 951–956.
- [72] Y.W. Chung, W.J. Lo, G.A. Somorjai, *Surf. Sci.* 64 (1977) 588–602.
- [73] Y. Uwamino, T. Ishizuka, H. Yamatera, *J. Electron Spectrosc. Relat. Phenom.* 34 (1984) 67–78.
- [74] M. Gorgoi, F. Schäfers, S. Svensson, N. Mårtensson, *J. Electron Spectrosc. Relat. Phenom.* 190 (2013) 153–158.
- [75] J.F. Moulder, W.F. Stickle, P.E. Sobol, K.D. Bomben, *Handbook of X Ray Photoelectron Spectroscopy*, Physical Electronics, Inc, Eden Prairie, Minnesota, USA, 1995, 0-9648124-1-X.
- [76] D. Neagu, G. Tsekouras, D.N. Miller, H. Menard, J.T.S. Irvine, *Nat. Chem.* 5 (2013) 916–923.
- [77] D. Neagu, T. Oh, D.N. Miller, H. Menard, S.M. Bukhari, S.R. Gamble, R.J. Gorte, J.M. Vohs, J.T.S. Irvine, *Nature Comm.* 6 (2015).
- [78] W. Qi, K. Xie, M. Liu, G. Wu, Y. Wang, Y. Zhanga, Y. Wu, *RSC Adv.* 4 (2014) 40494–40504.
- [79] N. Yao, V. Lordi, S.X.C. Ma, E. Dujardin, A. Krishnan, M.M.J. Treacy, T.W. Ebbesen, *J. Mater. Res.* 13 (1998) 2432–2437.
- [80] V.M. Gonzalez-Delacruz, F. Ternero, R. Pereñíguez, A. Caballero, J.P. Holgado, *Appl. Catal. A* 384 (2010) 1–9.
- [81] J.-P. Dacquin, D. Sellam, C. Batiot-Dupeyrat, A. Tougeri, D. Duprez, S. Royer, *ChemSustChem* 7 (2014) 631–637.
- [82] F. Wang, L. Xu, W. Shi, J. Zhang, K. Wu, Y. Zhao, H. Li, H.X. Li, G.Q. Xu, W. Chen, *Nano Res.* 10 (2017) 364–380.
- [83] J. Wei, E. Iglesia, *J. Phys. Chem. B.* 108 (2004) 4094–4103.
- [84] Y.T. Shah, T.H. Gardner, *Catal. Rev.* 56 (2014) 476–536.
- [85] Z.L. Zhang, V.A. Tsipouriari, A.M. Efstathiou, X.E. Verykios, *J. Catal.* 158 (1996) 51–63.
- [86] N. Wang, K. Shen, L. Huang, X. Yu, W. Qian, W. Chu, *ACS Catal.* 3 (2013) 1638–1651.
- [87] J. Wei, E. Iglesia, *J. Catalysis.* 225 (2004) 116–127.
- [88] Z. Zhang, X.E. Verykios, *Appl. Catal. A: Gen.* 138 (1996) 109–133.
- [89] V.A. Tsipouriari, X.E. Verykios, *Catal. Today* 64 (2001) 83–90.
- [90] S. Sokolov, E.V. Kondratenko, M.-Martina Pohl, U. Rodemerck, *Int. J. Hydrogen Energy* 38 (2013) 16121–16132.
- [91] N. Bion, F. Epron, D. Duprez, *V. Catalysis*, (2010) 1–55.
- [92] N. Bion, D. Duprez, *C. R. Chimie* 19 (2016) 1326–1336.